

Article

Construction of $\text{CoNi}_2\text{S}_4@\text{Ni(OH)}_2$ Nanosheet Structures for Asymmetric Supercapacitors with Excellent Performance

Yongli Tong ^{1,*}, Baoqian Chi ¹, Yu Jiang ¹ and Xiang Wu ^{2,*} 

¹ School of Science, Shenyang Ligong University, Shenyang 110159, China; baoqianchi@sylu.edu.cn (B.C.); jiangyu@sylu.edu.cn (Y.J.)

² School of Materials Science and Engineering, Shenyang University of Technology, Shenyang 110870, China

* Correspondence: tonyongli@sylu.edu.cn (Y.T.); wuxiang05@sut.edu.cn (X.W.)

Abstract: It is crucial for energy storage devices to construct electrode materials with excellent performance. However, enhancing energy density and cycling stability for supercapacitors is a significant challenge. We successfully synthesized $\text{CoNi}_2\text{S}_4@\text{Ni(OH)}_2$ nanosheets on the surface of Ni foam substrate by a two-step hydrothermal approach. The obtained products exhibit a remarkable areal capacitance of 1534 F g^{-1} at a current density of 1 A g^{-1} . Moreover, even after 10,000 cycles, the specific capacitance remains 90% of its initial value, highlighting the exceptional long-term stability and durability. Furthermore, an asymmetric supercapacitor (ASC) device incorporating the $\text{CoNi}_2\text{S}_4@\text{Ni(OH)}_2$ material shows remarkable electrochemical performance. It delivers an energy density of 58.5 mW h g^{-1} at a power density of 2700 W kg^{-1} . The outstanding performance mainly arises from the selection of materials, the design of the structure, and the synergistic interaction between the materials. The result suggests that this material holds great potential as an energy storage material.

Keywords: supercapacitors; $\text{CoNi}_2\text{S}_4@\text{Ni(OH)}_2$; energy density; composite structure; specific capacity



Academic Editor: Douglas Ivey

Received: 27 January 2025

Revised: 16 February 2025

Accepted: 18 February 2025

Published: 20 February 2025

Citation: Tong, Y.; Chi, B.; Jiang, Y.; Wu, X. Construction of $\text{CoNi}_2\text{S}_4@\text{Ni(OH)}_2$ Nanosheet Structures for Asymmetric Supercapacitors with Excellent Performance. *Batteries* **2025**, *11*, 83. <https://doi.org/10.3390/batteries11030083>

Copyright: © 2025 by the authors. Licensee MDPI, Basel, Switzerland. This article is an open access article distributed under the terms and conditions of the Creative Commons Attribution (CC BY) license (<https://creativecommons.org/licenses/by/4.0/>).

1. Introduction

The world is currently facing significant environmental and energy challenges [1–3]. These issues pose a serious threat to both human life and wildlife. To mitigate these problems, the development of green renewable energy sources has become essential [4–6]. Investing in green energy can help to reduce carbon footprints, create jobs, and promote energy independence, while preserving natural resources for future generations. Supercapacitors have garnered considerable interest due to their outstanding advantages over traditional batteries. Unlike conventional batteries, supercapacitors offer extremely fast charge/discharge rates, which make them an excellent choice for applications that demand rapid bursts of energy. Additionally, supercapacitors have an extended cycle life, which can endure hundreds of thousands to millions of cycles without significant degradation. Supercapacitors feature high power density, enabling them to deliver large amounts of power in a short time [7–10]. Moreover, supercapacitors are more environmentally friendly and have fewer safety concerns. Based on the charge storage mechanism, asymmetric supercapacitors are classified into two types. One is a double-layer capacitor, which stores energy by electrostatically adsorbing charges between the electrolyte and the interface of the electrode. During this process, ions gather on the surface of electrode, creating a double electric layer that facilitates energy storage. The other is a pseudocapacitor, where energy is stored through fast surface redox reactions, involving electron transfer between

the electrolyte and the electrode material. The material type is essential in determining the charge storage capacity. The advancement of these supercapacitors is crucial for meeting the increasing need for energy storage solutions. They are not only environmentally sustainable, but also efficient [11–14].

Transition metal sulfides, like Co_3S_4 and CoNi_2S_4 , have already been extensively studied as electrode materials, due to their outstanding electrochemical properties [15–17]. Among these, CoNi_2S_4 has been extensively researched. This material exhibits a high specific capacitance, primarily due to its extensive surface area, which allows for greater charge storage. Additionally, it can undergo reversible redox reactions when the charge–discharge reaction is repeated. This contributes to its high capacitance. These reactions, which involve the transfer of electrons between the electrolyte and the electrode, provide an additional mechanism for charge storage beyond just physical adsorption. Furthermore, the material's relatively high electrical conductivity is essential for boosting its performance. This enhanced conductivity facilitates the efficient movement of charge. Good conductivity improves the flow of charge, leading to a better rate capability. This means that the material can charge and discharge more quickly without significant loss of efficiency, which makes it ideal for high-power applications [18]. Li et al. [19] report the creation of r- CoNi_2S_4 nanosheets in transition metal dichalcogenides through a moderate-reduction method. The material demonstrated a remarkable improvement in conductivity and an increased number of active sites, which were mainly attributed to the abundant sulfur vacancies that were deliberately introduced. These vacancies are key to improving the electrochemical properties of the material, leading to better charge storage and faster electron transfer. The r- CoNi_2S_4 nanosheets, in particular, demonstrated a considerably higher specific capacitance, reaching 1117 C g^{-1} at 2 A g^{-1} . In addition, the device utilizing these nanosheets achieved an outstanding energy density of 55.4 Wh kg^{-1} at a power density of 8 kW kg^{-1} , along with 80% capacitance retention after 10,000 cycles. However, like many transition metal sulfides, CoNi_2S_4 experiences volume expansion during cycling, which can lead to mechanical stress and degradation of the material, reducing its long-term performance.

To improve this drawback, a composite structure has been designed. When transition metal sulfides are combined with other components, the composite structure can provide better mechanical stability, reducing the effects of volume changes and improving cycling performance. Additionally, by combining these materials with conductive materials, the resulting composite improves the overall electrical conductivity, facilitating better electron transport and faster charge/discharge rates [20,21]. The combination of different materials can lead to a synergistic effect, where the properties of the individual components complement each other [22–24]. Thus, composites can be specifically engineered to improve multiple aspects of supercapacitor performance, making them a highly versatile and effective solution. In this work, a hybrid $\text{CoNi}_2\text{S}_4@\text{Ni(OH)}_2$ electrode is fabricated on the surface of nickel foam through a two-step hydrothermal approach. The composite material exhibits outstanding electrochemical performance. The assembled device also possesses excellent power density and energy density.

2. Experimental Section

2.1. Preparation of Materials

Cobalt nitrate, nickel nitrate, ammonium fluoride, urea, and nickel foam were sourced from Aladdin. All chemical reagents were used without any modifications. Before the experiment, a piece of Ni foam ($4 \times 4 \times 0.3 \text{ cm}$) was immersed in a 1 M hydrochloric acid solution for half an hour to remove surface impurities, then rinsed three times with ethanol and deionized (DI) water, respectively. Finally, it was placed in an oven to dry at 60°C overnight.

Total volumes of 60 mL DI water, 3 mmol NH₄F, 2 mmol Co(NO₃)₂·6H₂O, 7 mmol urea, and 1 mmol Ni(NO₃)₂·6H₂O were placed in a beaker, followed by magnetic stirring. When the solution became clear at room temperature, stirring was stopped. The prepared mixture was subsequently introduced into an autoclave of 100 mL, to which prepared Ni foam was added. The autoclave was heated at 120 °C for 6 h in an oven, to facilitate the reaction. After the heating process was complete, the product was left to cool to room temperature. The product was then washed thoroughly with ethanol and DI water multiple times to eliminate any remaining impurities, resulting in the formation of the cobalt–nickel precursor.

After that, 0.40 g Na₂S and the as-prepared sample above, along with 40 mL DI water, were transferred to an autoclave, where they were heated at 120 °C for 4 h. The sample was dried according to the steps mentioned above, to obtain the CoNi₂S₄ product. Finally, 0.12 g of urea, 0.29 g of Ni(NO₃)₂·6H₂O, and 60 mL of DI water were mixed thoroughly to obtain clear solution. The prepared CoNi₂S₄ sample was then immersed in the mixture and heated at 100 °C for 8 h. CoNi₂S₄@Ni(OH)₂ samples were successfully obtained. The average mass loading on the nickel foam was approximately 2.32 mg cm⁻².

2.2. Morphology and Structure Characterization

The structural features of the products were analyzed through scanning electron microscopy (SEM, Sigma500 field emission, ZEISS, Oberkochen, Germany). X-ray diffraction (XRD) was performed with a BRUKER D8 X-ray diffractometer(BRUKER, Karlsruhe, Germany), utilizing Cu K α radiation ($\lambda = 1.5406 \text{ \AA}$). The elemental composition and structural details were examined through X-ray photoelectron spectroscopy (XPS, ESCALAB250, Thermo Fisher Scientific, Waltham, MA, USA).

2.3. Fabrication of ASC Device

A mixture of activated carbon, acetylene black, and polytetrafluoroethylene (PTFE), in a mass ratio of 7:2:1, was applied to the surface of the treated nickel foam with a diameter of 1 cm, followed by heating at 80 °C for 24 h. The carbon electrode obtained as described above was used as the cathode of the ASC, and the CoNi₂S₄@Ni(OH)₂ product served as the cathode. The electrolyte was bended by first heating 50 mL of deionized (DI) water to 95 °C. Then, 5 mg of PVA and 5 g of KOH were added gradually. The solution was stirred until it became clear. A piece of NKK paper was used to separate the anode and cathode to form a sandwich structure. The mass ratio of the anode and cathode can be determined using the following formula, based on charge balance [25]:

$$m^+ / m^- = C_- \times V_- / C_+ \times V_+ \quad (1)$$

2.4. Electrochemical Characterization

A range of electrochemical tests were carried out on an electrochemical workstation (Shanghai Chenhua CHI660e, Shanghai Chenhua Instrument Co., Ltd., Shanghai, China) to characterize the material's performance. They included Galvanostatic Charge–Discharge (GCD) tests, Electrochemical Impedance Spectroscopy (EIS) and Cyclic Voltammetry (CV). Specific capacitance (C_s) was obtained using the following formula [26,27]:

$$C_s = I\Delta t / mV \quad (2)$$

The energy density (E) and power density (P) of the ASC were constructed by the following formula:

$$E = 1/2C_s(\Delta V)^2 \quad (3)$$

$$P = 3600E/t \quad (4)$$

in which I serves as current density, and m stands for the mass of the electrode.

3. Results and Discussion

The phase component of the $\text{CoNi}_2\text{S}_4@\text{Ni(OH)}_2$ sample was analyzed by XRD; the results are shown in Figure 1a. The diffraction peaks at 44.5° , 51.8° , and 76.4° correspond to those characteristic of nickel foam (JCPDS no. 04-0850). These peaks indicate that the structure of the material is consistent with the well-established crystallographic patterns of nickel foam. The peaks at 38.2° , 47.2° , 50.3° , 55.1° , and 68.9° correspond well to the (400), (422), (511), (440), and (444) planes of CoNi_2S_4 (JCPDS no. 86-2247). The peaks observed at 33.2° , 38.6° , 52.1° , 59.3° , and 73.0° are attributed to the specific crystallographic planes of Ni(OH)_2 , namely the (100), (011), (012), (110), and (201) planes, respectively. These peaks serve as clear indicators of the presence of Ni(OH)_2 within the material, confirming its formation and crystallinity. Each of these diffraction angles corresponds to a distinct plane in the crystal structure of Ni(OH)_2 , providing valuable information about its phase and orientation.

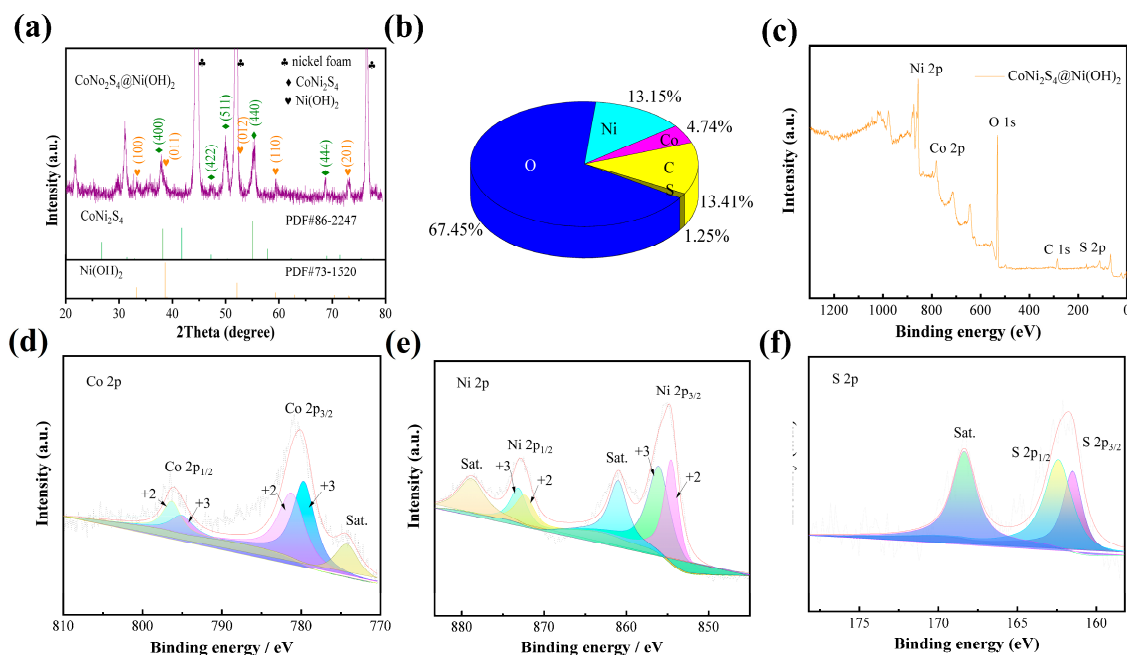


Figure 1. (a) XRD patterns of $\text{CoNi}_2\text{S}_4@\text{Ni(OH)}_2$. (b) Element content pie chart. (c) XPS survey. (d) Co 2p. (e) Ni 2p. (f) S 2p.

The surface chemical states of the $\text{CoNi}_2\text{S}_4@\text{Ni(OH)}_2$ sample were determined by XPS. Figure 1b shows the proportions of the five elements, as follows: O—67.45%, Ni—13.15%, Co—4.74%, C—13.41%, and S—1.25%. The survey spectrum in Figure 1c indeed confirms the presence of these elements. As shown in Figure 1d, the spectra exhibit two characteristic spin-orbit doublet peaks, which correspond to Co 2p_{3/2} and Co 2p_{1/2}, with binding energies of 796.1 eV and 780.2 eV, respectively. These peaks suggest the presence of cobalt in its characteristic oxidation states, with the measured binding energies closely matching expectations for Co 2p electron states in cobalt-containing compounds. The spin-orbit splitting value is approximately 15.9 eV, which is attributed to the presence of Co^{3+} and Co^{2+} ionic states [28,29]. The energies at 778.2 and 792.6 eV are attributed to Co^{3+} , while the energies at 796.4 and 780.9 eV are associated with Co^{2+} .

The Ni 2p spectra (Figure 1e) exhibit four peaks, at 855.4, 873.4, 857.1, and 875.6 eV, corresponding to Ni^{2+} and Ni^{3+} [30,31]. Additionally, two satellite peaks at 862.1 and 880.4 eV can be attributed to the higher oxidation state. Among the four peaks shown

on the Ni spectra, the two energies of 872.8 eV and 854.9 eV are the orbital peaks, while the energies at 862.1 and 880.4 eV are satellite peaks. The peaks at 855.4 and 873.4 eV are attributed to Ni^{2+} , while the energies at 857.3 and 875.7 eV correspond to Ni^{3+} . The S 2p spectra display two orbital peaks, at 156.6 eV and 157.2 eV, corresponding to S 2p_{3/2} and S 2p_{1/2}, respectively.

The morphology of the prepared samples is illustrated in Figure 2. It can be seen that the nanosheets evenly cover the whole surface of the Ni foam (Figure 2a). From the high-magnification SEM image in Figure 2b, it can be seen that the thickness of the CoNi_2S_4 product is approximately 20 nm, and nanowires grow uniformly at the edges of the nanosheets. This means that the sample has a larger specific surface area compared to pure sheets. Figure 2c,d show the uniform morphology of Ni(OH)_2 directly grown on Ni foam. The average thickness of its nanosheets is around 10 nm. Figure 2e,f show how the Ni(OH)_2 nanosheets are uniformly attached to the surface of the CoNi_2S_4 material. The $\text{CoNi}_2\text{S}_4@\text{Ni(OH)}_2$ nanosheets reinforce the electrode structure and exhibit a large specific surface area, suggesting excellent electrochemical performance.

The electrochemical data of the prepared products were evaluated through a traditional three-electrode system, with a 3 M potassium hydroxide solution serving as the electrolyte. Figure 3a shows the CV curves of the three samples, Ni(OH)_2 , CoNi_2S_4 , and $\text{CoNi}_2\text{S}_4@\text{Ni(OH)}_2$, obtained at 50 mV s⁻¹. The clearly defined redox peaks suggest that the materials exhibit battery-type behavior. The $\text{CoNi}_2\text{S}_4@\text{Ni(OH)}_2$ samples show the largest area among the three materials, which suggests a significant improvement in capacitance following the formation of the composite. This improvement can be attributed to the shortening of the electron and ion transport pathways, as well as the increase in specific surface area following the formation of the composite material. The large surface area provides abundant active sites, allowing for more efficient electrochemical reactions during charge and discharge cycles. With more available sites, the material can accommodate a greater number of ions, enhancing its overall capacitance. Additionally, the shorter transport pathways facilitate faster electron and ion movement, which allow for more efficient electron and ion movement. This combination enhances the material's overall electrochemical performance, leading to better charge storage capacity, faster charge–discharge rates, and improved energy efficiency.

Figure 3b exhibits the GCD curves of the $\text{CoNi}_2\text{S}_4@\text{Ni(OH)}_2$, CoNi_2S_4 , and Ni(OH)_2 materials at 1 A g⁻¹. The curves show distinct plateaus, which correspond to the charge–discharge redox processes of the electrode, consistently with the CV curves. The $\text{CoNi}_2\text{S}_4@\text{Ni(OH)}_2$ material possesses the longest discharge time, suggesting that it has the highest capacitance. Therefore, it shows significant improvement compared to the CoNi_2S_4 and Ni(OH)_2 materials. This suggests that the composite material is more efficient at storing and releasing charge.

Nyquist plots of three electrodes were created to further assess the kinetic performance, as shown in Figure 3c. The linear segment indicates the rate at which ions are transported between the electrolyte and the electrode surface. A greater slope of the line signifies a more rapid ion transport rate. The figure shows that the $\text{CoNi}_2\text{S}_4@\text{Ni(OH)}_2$ material possesses a faster rate compared to the other two materials. The equivalent resistance of the $\text{CoNi}_2\text{S}_4@\text{Ni(OH)}_2$ sample at the intersection with the x-axis is approximately 0.65 Ω, which is smaller than that of the other two materials.

CV curves were created to further assess the performance of the $\text{CoNi}_2\text{S}_4@\text{Ni(OH)}_2$ sample at various scan rates, as shown in Figure 3d. As the scan rate increases, the general shape of the curve stays largely unchanged, suggesting that the material maintains a stable electrochemical behavior and can function effectively across a range of operating conditions. Moreover, with an increase in scan rate, the redox peaks display a slight shift

in both directions. This shift is often attributed to limitations in ion diffusion at higher scan rates, where the material may experience slight delays in the movement of ions to the active sites.

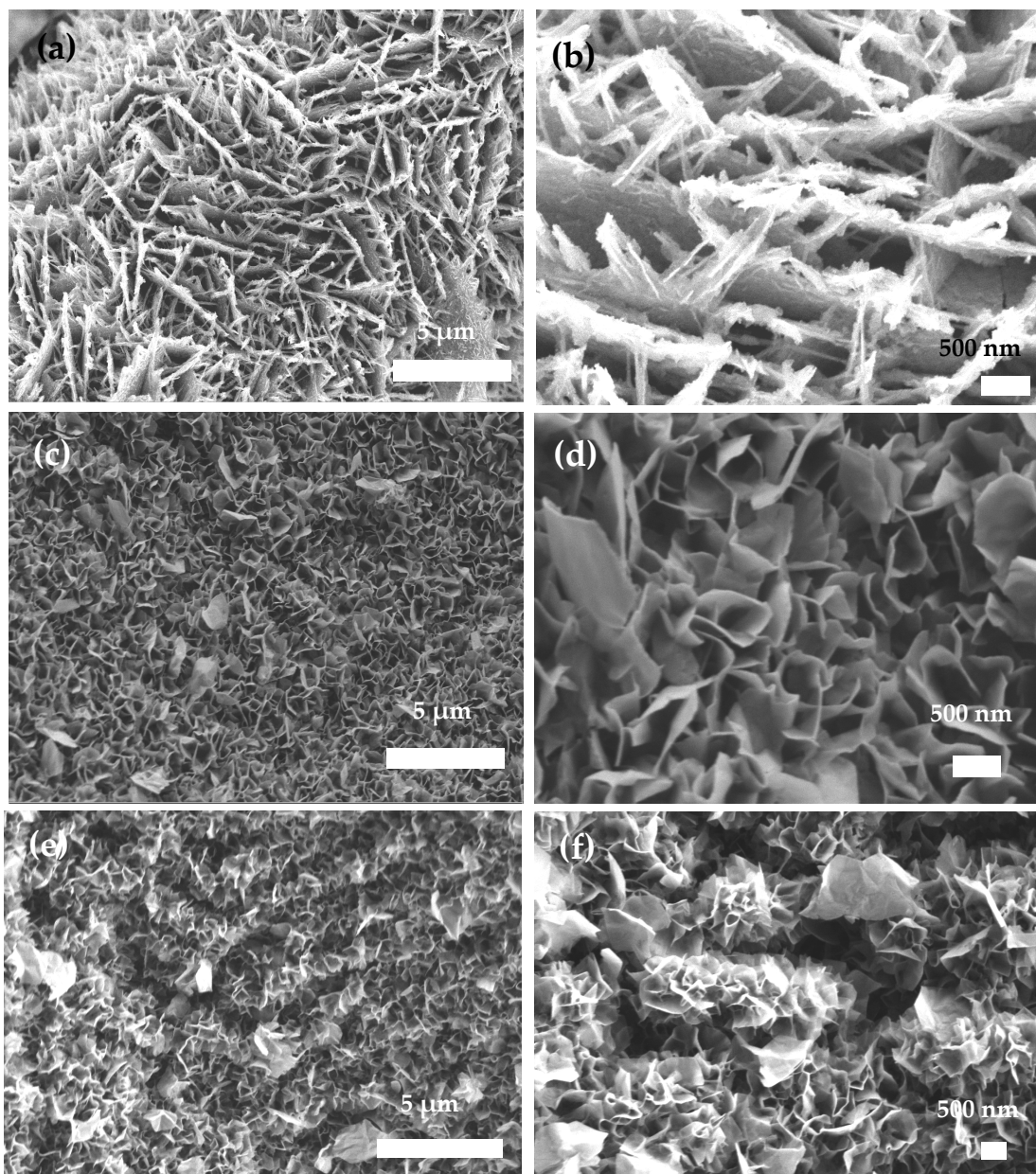


Figure 2. SEM images of samples: (a,b) CoNi_2S_4 material; (c,d) $\text{Ni}(\text{OH})_2$ sample; (e,f) $\text{CoNi}_2\text{S}_4@\text{Ni}(\text{OH})_2$ sample.

From these CV curves, the charge–discharge mechanism is further revealed in Figure 3e. CV curves serve as a powerful method for analyzing the reaction kinetics of the as-prepared samples. The equation for this is presented below:

$$i = av^b \quad (5)$$

In this equation, i serves as the current, v stands for scan rate, and b indicates the reaction kinetics speed.

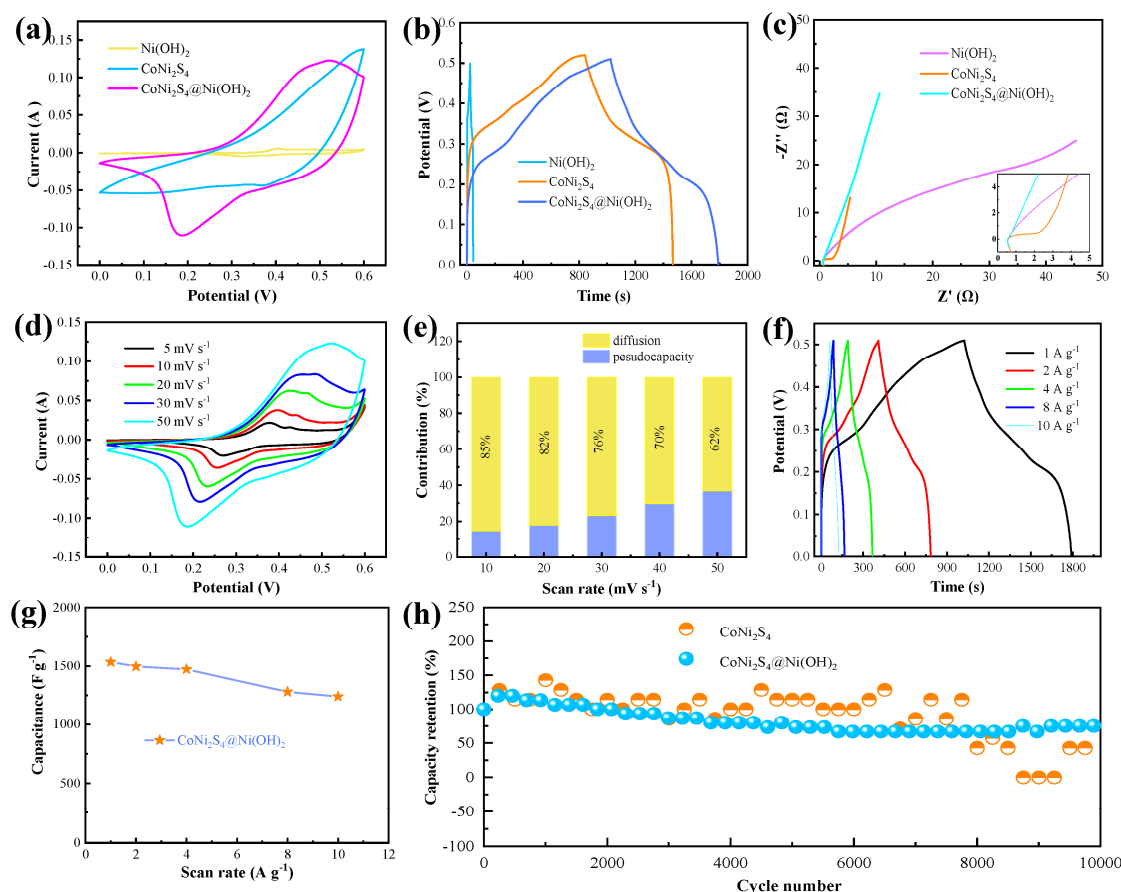


Figure 3. Electrochemical performance: (a) CV curves of prepared samples at scan rate of 50 mV/s. (b) GCD curves of prepared samples at 1 A g⁻¹. (c) Nyquist plots of prepared samples. (d) CV curves at different scan rates. (e) Contribution ratio. (f) GCD curves at different current densities. (g) Capacitance at different scan rates. (h) Cycling performance.

To explore the proportional contribution of the two charge storage mechanisms, surface capacitance and diffusion capacitance, the following formula is used:

$$i = k_1 v + k_2 v^{1/2} \quad (6)$$

where the values of k_1 and k_2 can be determined from the CV curves. The charge storage caused by diffusion reaches 85% at 10 mV s⁻¹, and decreases continuously when the scan rate increases. The charge storage caused by pseudocapacitance increases continuously with an increase in scan rate.

The charging and discharging portions of the GCD curves are basically symmetrical, indicating that the material has high recoverability. According to Equation (2), the specific capacitance is calculated to be 1534 F g⁻¹, based on the discharge time at 1 A g⁻¹ (Figure 3f). The material maintains a capacitance retention rate of up to 80%, even at a high current density of 10 A g⁻¹, which indicates that the phenomenon of polarization of the material is not significant. As observed from Figure 3g, the curve drops gently. This indicates that the specific capacitance gradually decreases with an increase in current density. This demonstrates the material's excellent ability to withstand rapid charge and discharge cycles.

The stability and durability of the CoNi₂S₄@Ni(OH)₂ electrode material were explored through long-cycle testing, as shown in Figure 3h. As the number of cycles increases, the curve shows an upward trend, reaching a maximum value at approximately 200 cycles. This indicates the activation process of the material. The electrode material continuously absorbs the electrolyte, leading to an increase in active sites, more particles participating in

the reaction, and a rise in specific capacitance. Subsequently, the curve shows a downward trend, which is due to the repeated adsorption/desorption of the material, causing volume expansion or collapse, and even convergence in some cases. This leads to a gradual reduction in reaction sites. After 10,000 cycles, the specific capacitance retains 90% of its original value, demonstrating impressive cycling stability. This excellent retention indicates that the material undergoes minimal degradation during the repeated redox process, which is a key factor for long-term performance. After the composite formation, it is evident that the material's stability is significantly improved. This is because sulfides have poor stability. By coating them with a layer of Ni(OH)₂ material, this can alleviate issues, such as volume expansion and material collapse, caused by the repeated reversible redox process.

To explore the applicability of the CoNi₂S₄@Ni(OH)₂ electrode material, a device was assembled. As shown in Figure 4a, the shape of the curves remains largely unchanged when the operating voltage varies from 1.2 to 1.6 V. This indicates that the device functions normally. Meanwhile, the shape of the curve remains largely unchanged when the scan rate varies between 10 and 100 mV s⁻¹ (Figure 4b). This suggests that the material possesses a low polarization rate and excellent electrochemical performance [32,33].

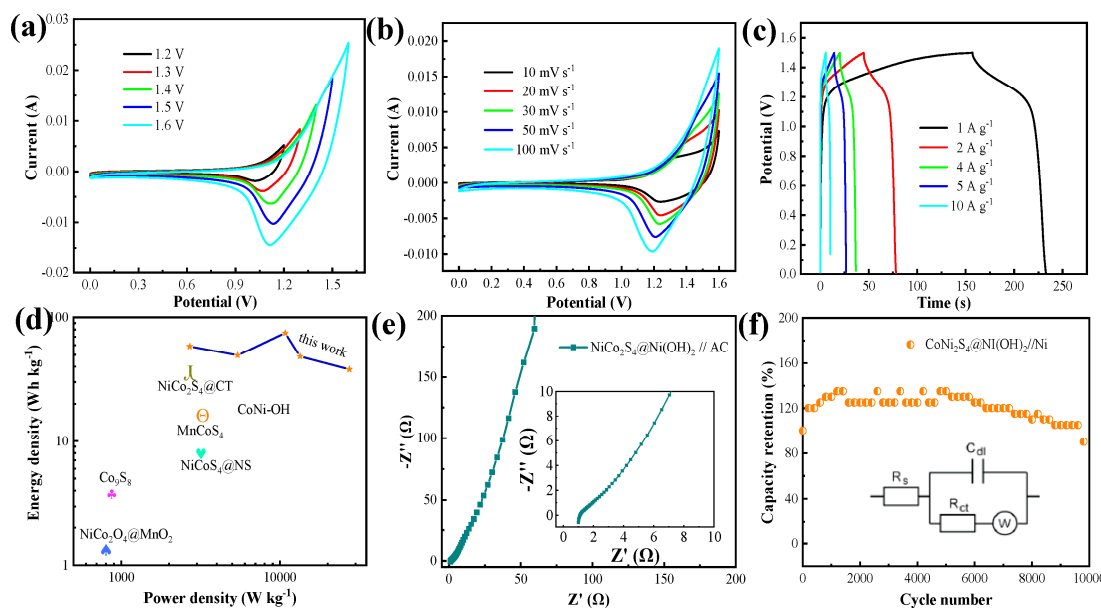


Figure 4. Electrochemical performance of device: (a) CV curves at different scan rates. (b) CV curves at 50 mV/s. (c) GCD curves at different current densities. (d) Nyquist plots. (e) Ragone plot. (f) Cycling performance.

It can be observed that the GCD curve shows some deviation in the charge and discharge times, which means lower Coulombic efficiency. This may be caused by the following factors: 1. Charge leakage and electrode polarization; 2. Inconsistent electrochemical kinetics between the anode and cathode. The kinetic rate of the CoNi₂S₄@Ni(OH)₂ material is slower than that of the carbon material used for the cathode; 3. The use of a separator and binder during the device assembly process increases the resistance of the electrode and hinders the transfer of electrons and charge; 4. At high potentials, the ion transport rate in the electrolyte slows down, requiring a longer time for charge accumulation. The specific capacitance of the device is determined to be 52.4 F g⁻¹ at 1 A g⁻¹, according to Figure 4c. To further assess the device's performance, its energy density and power density were calculated by Equations (2) and (3). The energy density of the device is calculated to be 58.5 Wh kg⁻¹, while the power density reaches 2700 W kg⁻¹. These calculations highlight the material's ability in terms of storing and delivering energy efficiently, making

it a match in terms of both high power output and substantial energy storage. As shown in Figure 4d, the values for these are higher in this work than in some previously reported data [34–39]. Table 1 shows a data comparison between this sample and other materials. Figure 4e shows that the equivalent resistance of the device is about $1\ \Omega$. The results of EIS and inset in Figure 4e show that the device possesses a small equivalent resistance and a fast transmission speed. The cyclic characteristic of the device is also an important indicator. The device can still maintain a specific capacitance that equals 90% of the initial capacitance after 10,000 cycles, which reveals its outstanding electrochemical properties.

Table 1. A comparison of the current device with previously reported electrode materials.

| Materials | Energy Density (Wh·kg ⁻¹) | Power Density (W·kg ⁻¹) | Capacitance (F g ⁻¹) | Stability | Refs. |
|---|--|--|-------------------------------------|------------------------|-----------|
| NiCo ₂ S ₄ @CT | 36.1 | 798 | 59.2 | 89.2% (3000 cycles) | [34] |
| NiCo ₂ S ₄ @NS | 25.5 | 334 | 71.6 | 85.6% (4000 cycles) | [35] |
| MnCo ₂ S ₄ | 31.3 | 800 | 41.2 | 89% (5000 cycles) | [36] |
| Co ₉ S ₈ | 13.3 | 1110 | 48.4 | 73% (4000 cycles) | [37] |
| NiCo ₂ O ₄ @MnO ₂ | 5.8 | 175 | 31.3 | 93% (3000 cycles) | [38] |
| CoNi-OH | 34.2 | 800 | 62.5 | 70% (6000 cycles) | [39] |
| CoNi ₂ S ₄ @Ni(OH) ₂ | 58.5 | 2700 | 52.4 | 90% (10,000 cycles) | This work |

4. Conclusions

In summary, we prepared CoNi₂S₄@Ni(OH)₂ samples using a straightforward hydrothermal synthesis method. Ni(OH)₂ nanosheets are interspersedly grown on the surface of CoNi₂S₄ nanosheets, significantly enhancing the material's electrochemical performance. This approach not only simplifies the production process, but also yields a material with exceptional electrochemical performance, exhibiting a specific capacitance of 1534 F g^{-1} . The assembled device still retains 90% of the initial specific capacitance after 10,000 cycles, and it can achieve an energy density of 58.5 Wh kg^{-1} at 2700 W kg^{-1} . Through this innovative design, this method not only effectively enhances the material's specific surface area and shortens the reaction path, but also strengthens the surface strength of the sulfide, greatly improving cycling performance.

Author Contributions: Conceptualization, Y.T., B.C., Y.J. and X.W.; Software, B.C. and Y.J.; Validation, B.C.; Formal analysis, Y.T. and X.W.; Investigation, B.C.; Resources, X.W.; Data curation, Y.T. and Y.J.; Writing—original draft, Y.T.; Writing—review & editing, X.W.; Project administration, Y.T. and X.W.; Funding acquisition, Y.T. All authors have read and agreed to the published version of the manuscript.

Funding: The work is supported by the Special Fund of Basic scientific Research Business expenses of undergraduate universities in Liaoning Province (LJ212410144004) from Liaoning Provincial Department of Education, and the College student innovation and entrepreneurship project of Shenyang Ligong University (X202410144013) from Shenyang Ligong University.

Data Availability Statement: Data are contained within the article.

Conflicts of Interest: The authors declare no conflicts of interest.

References

- Zhang, Y.; Chen, Y.; Liang, K.; Zhang, Y.; Wang, D.; Wang, W.; Wang, J.; Mitsuzaki, N.; Chen, Z. Synthesis of nickel cobalt sulfide electrode materials for high-performance asymmetric supercapacitors. *J. Energy Storage* **2025**, *109*, 115176. [[CrossRef](#)]
- Iqbal, M.; Saykar, N.G.; Alegaonkar, P.S.; Mahapatra, S.K. Synergistically modified WS₂@PANI binary nanocomposite-based all-solid-state symmetric supercapacitor with high energy density. *New J. Chem.* **2022**, *46*, 7043–7054. [[CrossRef](#)]
- Yao, S.Y.; Jiao, Y.; Lv, C.D.; Kong, Y.; Ramakrishna, S.; Chen, G. Lattice-strain engineering of CoOOH induced by NiMn-MOF for high-efficiency supercapacitor and water oxidation electrocatalysis. *J. Colloid Interf. Sci.* **2022**, *623*, 1111–1121. [[CrossRef](#)]
- De Adhikari, A.; Shauloff, N.; Turkulets, Y.; Shalish, I.; Jelinek, R. Tungsten-Disulfide/Polyaniline High Frequency Supercapacitors. *Adv. Electron. Mater.* **2021**, *7*, 2100025. [[CrossRef](#)]
- Crisci, M.; Boll, F.; Merola, L.; Pflug, J.J.; Liu, Z.M.; Gallego, J.; Lamberti, F.; Gatti, T. Nanostructured 2D WS₂@PANI nanohybrids for electrochemical energy storage. *Front. Chem.* **2022**, *10*, 1000910. [[CrossRef](#)]
- Tong, Y.; Liu, X.; Qi, D.; Chi, B. Constructing high performance supercapacitor electrode through PPy decorated Co₃O₄@CoMoO₄ sandwich structure. *J. Energy Storage* **2024**, *97*, 112798. [[CrossRef](#)]
- Shi, C.; Wang, Y.; Kulaots, I.; Zhu, H.; Sheldon, B. Water-in-Salt Battery Electrolyte for High-Voltage Supercapacitors: A Fundamental Study on Biomass and Carbon Fiber Electrodes. *J. Electrochem. Soc.* **2024**, *171*, 110526. [[CrossRef](#)]
- Yao, S.Y.; Jiao, Y.; Sun, S.F.; Wang, L.X.; Li, P.Y.; Chen, G. Vertically Co-oriented Mn-Metal–Organic Framework grown on 2D cation-intercalated manganese oxide via a self-sacrificing template process for a high-performance asymmetric supercapacitor. *ACS Sustain. Chem. Eng.* **2020**, *8*, 3191–3199. [[CrossRef](#)]
- Li, R.Y.; Xu, S.L.; Ai, Z.Q.; Qi, J.G.; Wu, F.F.; Zhao, R.D.; Zhao, D.P. Interface Engineering Accelerated Surface Reconstruction for Electrocatalytic Water Splitting and Energy Storage Device through Hybrid Structured ZnCo₂O₄@NiCo-LDH Nanocomposite. *Int. J. Hydrog. Energy* **2024**, *91*, 867–876. [[CrossRef](#)]
- Li, R.Y.; Shen, X.Y.; Li, J.; Zhao, D.P.; Zhao, R.D.; Wu, F.F. Enhanced Electrochemical Performance of NiCo-Layered Double Hydroxides: Optimal Synthesis Conditions and Supercapacitor Applications. *Adv. Sustain. Syst.* **2024**, *2400753*.
- Yao, S.Y.; Ramakrishna, S.; Chen, G. Recent advances in metal–organic frameworks based on electrospinning for energy storage. *Adv. Fiber Mater.* **2023**, *5*, 1592–1617. [[CrossRef](#)]
- Dhandapani, E.; Thangarasu, S.; Ramesh, S.; Ramesh, K.; Vasudevan, R.; Duraisamy, N. Recent development and prospective of carbonaceous material, conducting polymer and their composite electrode materials for supercapacitor—A review. *J. Energy Storage* **2022**, *52*, 104937. [[CrossRef](#)]
- Zhang, M.; Du, H.; Wei, Z.; Zhang, X.; Wang, R. Ultrafast microwave synthesis of nickel-cobalt sulfide/graphene hybrid electrodes for high-performance asymmetrical supercapacitors. *ACS Appl. Energy Mater.* **2021**, *4*, 8262–8274.
- Zhu, J.; Wu, Q.; Li, J. Review and prospect of Mn₃O₄-based composite materials for supercapacitor electrodes. *ChemistrySelect* **2020**, *5*, 10407–10423. [[CrossRef](#)]
- Chen, L.; Wan, J.f.; Fan, L.; Wei, Y.; Zou, J.l. Construction of CoNi₂S₄ hollow cube structures for excellent performance asymmetric supercapacitors. *Appl. Surf. Sci.* **2021**, *570*, 151174. [[CrossRef](#)]
- Aisha, S.; Nagaraju, D.H.; Mahesh, P. High-energy-density asymmetric supercapacitor based on layered-double-hydroxide-derived CoNi₂S₄ and eco-friendly biomass-derived activated carbon. *Energy Fuels* **2022**, *36*, 13286–13295.
- Zhu, J.; Han, C.; Song, X. Facile synthesis of novel CoNi₂S₄/carbon nanofibers composite for high-performance supercapacitor. *Mater. Chem. Phys.* **2022**, *283*, 126038. [[CrossRef](#)]
- Patil, S.J.; Kim, J.H.; Lee, D.W. Self-assembled Ni₃S₂//CoNi₂S₄ nanoarrays for ultra high-performance supercapacitor. *Chem. Eng. J.* **2017**, *322*, 498–509. [[CrossRef](#)]
- Li, Z.; Zhao, D.; Xu, C.; Ning, J.; Zhong, Y.; Zhang, Z.; Wang, Y.; Hu, Y. Reduced CoNi₂S₄ nanosheets with enhanced conductivity for high-performance supercapacitors. *Electrochim. Acta* **2018**, *278*, 33–41. [[CrossRef](#)]
- Visakh, C.; Mohan, V.; Rakhi, R.B. WS₂/Conducting polymer nanocomposite-based flexible and binder-free electrodes for high-performance supercapacitors. *Electrochim. Acta* **2024**, *498*, 144657.
- Wang, J.; Zheng, F.; Yu, Y.; Hu, P.; Li, M.; Wang, J.; Fu, J.; Zhen, Q.; Bashir, S.; Liu, J.L. Symmetric supercapacitors composed of ternary metal oxides (NiO/V₂O₅/MnO₂) nanoribbon electrodes with high energy storage performance. *Chem. Eng. J.* **2021**, *426*, 131804. [[CrossRef](#)]
- Chevulamaddi, H.; Kalagadda, V.R. The improved electrochemical performance of MnO₂ nanorods decorated with polyaniline as efficient electrode towards high performance supercapacitors. *J. Mater. Sci. Mater. Electron.* **2024**, *35*, 2273. [[CrossRef](#)]
- Yue, T.; Shen, B.; Gao, P. Carbon material/MnO₂ as conductive skeleton for supercapacitor electrode material: A review. *Renew. Sustain. Energy Rev.* **2022**, *158*, 112131. [[CrossRef](#)]
- Song, M.; Zhou, Y.; Ren, X.; Wan, J.; Du, Y.; Wu, G.; Ma, F. Biowaste-based porous carbon for supercapacitor: The influence of preparation processes on structure and performance. *J. Colloid Interface Sci.* **2019**, *535*, 276–286. [[CrossRef](#)] [[PubMed](#)]
- Agyapong, A.D.; Cooley, K.A.; Mohney, S.E. Reactivity of contact metals on monolayer WS₂. *J. Appl. Phys.* **2020**, *128*, 055306. [[CrossRef](#)]

26. Zubairi, H.; Lu, Z.; Zhu, Y.; Reaney, I.M.; Wang, G. Current development, optimisation strategies and future perspectives for lead-free dielectric ceramics in high field and high energy density capacitors. *Chem. Soc. Rev.* **2024**, *53*, 10761–10790. [[CrossRef](#)]
27. Yang, W.; Wang, P.; Tu, Z.; Hou, L.; Yan, L.; Jiang, B.; Zhang, C.; Huang, G.; Yang, F.; Li, Y. Heteroatoms-doped hierarchical porous carbon with multi-scale structure derived from petroleum asphalt for high-performance supercapacitors. *Carbon* **2022**, *187*, 338–348. [[CrossRef](#)]
28. Zhang, M.; Du, H.; Wei, Z.; Zhang, X.; Wang, R. Facile electrodeposition of Mn-CoP nanosheets on Ni foam as high-rate and ultrastable electrodes for supercapacitors. *ACS Appl. Energy Mater.* **2022**, *5*, 186–195. [[CrossRef](#)]
29. Luo, L.; Lan, Y.; Zhang, Q.; Deng, J.; Luo, L.; Zeng, Q.; Gao, H.; Zhao, W. A review on biomass-derived activated carbon as electrode materials for energy storage supercapacitors. *J. Energy Storage* **2022**, *55*, 105839. [[CrossRef](#)]
30. Shah, S.S. Biomass-Derived Carbon Materials for Advanced Metal-Ion Hybrid Supercapacitors: A Step Towards More Sustainable Energy. *Batteries* **2024**, *10*, 168. [[CrossRef](#)]
31. Sun, L.; Zhuo, K.; Chen, Y.; Du, Q.; Zhang, S.; Wang, J. Ionic Liquid-Based Redox Active Electrolytes for Supercapacitors. *Adv. Funct. Mater.* **2022**, *32*, 2203611. [[CrossRef](#)]
32. Liu, R.; Wang, J.-X.; Yang, W.-D. Hierarchical Porous Heteroatoms—Co-Doped Activated Carbon Synthesized from Coconut Shell and Its Application for Supercapacitors. *Nanomaterials* **2022**, *12*, 3504. [[CrossRef](#)] [[PubMed](#)]
33. Li, Y.; Zhang, D.; Zhang, Y.; He, J.; Wang, Y.; Wang, K.; Xu, Y.; Li, H.; Wang, Y. Biomass-derived microporous carbon with large micropore size for high-performance supercapacitors. *J. Power Sources* **2020**, *448*, 227396. [[CrossRef](#)]
34. Hao, L.; Shen, L.; Wang, J.; Xu, Y.; Zhang, X. Hollow NiCo₂S₄ nanotube arrays grown on carbon textile as a self-supported electrode for asymmetric supercapacitors. *RSC Adv.* **2016**, *6*, 9950–9957. [[CrossRef](#)]
35. Wu, Z.; Pu, X.; Ji, X.; Zhu, Y.; Jing, M.; Chen, Q.; Jiao, F. High energy density asymmetric supercapacitors from mesoporous NiCo₂S₄ nanosheets. *Electrochim. Acta* **2015**, *174*, 238–245. [[CrossRef](#)]
36. Liu, S.; Jun, S. Hierarchical manganese cobalt sulfide core–shell nanostructures for high-performance asymmetric supercapacitors. *J. Power Sources* **2017**, *342*, 629–637. [[CrossRef](#)]
37. Mao, X.; Wang, Z.; Kong, W.; Wang, W. Nickel foam supported hierarchical Co₉S₈ nanostructures for asymmetric supercapacitors. *New J. Chem.* **2017**, *41*, 1142–1148. [[CrossRef](#)]
38. Kuang, M.; Wen, Z.; Guo, X.; Zhang, S.; Zhang, Y. Engineering firecracker-like beta-manganese dioxides@spinel nickel cobaltates nanostructures for high-performance supercapacitors. *J. Power Sources* **2014**, *270*, 426–433. [[CrossRef](#)]
39. Tang, Y.; Liu, Y.; Yu, S.; Guo, W.; Mu, S.; Wang, H.; Zhao, Y.; Hou, L.; Fan, Y.; Gao, F. Template-free hydrothermal synthesis of nickel cobalt hydroxide nanoflowers with high performance for asymmetric supercapacitor. *Electrochim. Acta* **2015**, *161*, 279–289. [[CrossRef](#)]

Disclaimer/Publisher’s Note: The statements, opinions and data contained in all publications are solely those of the individual author(s) and contributor(s) and not of MDPI and/or the editor(s). MDPI and/or the editor(s) disclaim responsibility for any injury to people or property resulting from any ideas, methods, instructions or products referred to in the content.